Geochemistry, Geophysics, Geosystems®

AGU ADVANCING EARTH AND SPACE SCIENCE

RESEARCH ARTICLE
10.1029/2021GC009987

Key Points:

- Deformation in the Rocky Mountain Front is highly correlated with high Δt^*
- Laramide-Style deformation may be caused by variations in lithospheric strength and thickness
- Stress may be localized in weaker lithosphere to form Laramide-style ranges

Supporting Information:

Supporting Information may be found in the online version of this article.

Correspondence to:

Z. Zhu,
zhu00064@umn.edu

Citation:

Zhu, Z., Bezada, M. J., Byrnes, J. S., & Ford, H. A. (2021). Evidence for stress localization caused by lithospheric heterogeneity from seismic attenuation. *Geochemistry, Geophysics, Geosystems*, *22*, e2021GC009987. https://doi.org/10.1029/2021GC009987

Received 17 JUN 2021
Accepted 29 OCT 2021

Evidence for Stress Localization Caused by Lithospheric Heterogeneity From Seismic Attenuation

Zhao Zhu[1], Maximiliano J. Bezada[1], Joseph S. Byrnes[1,2], and Heather A. Ford[3]

[1]Department of Earth & Environmental Sciences, University of Minnesota, Twin Cities, MN, USA, [2]Now at Northern Arizona University, Flagstaff, AZ, USA, [3]Department of Earth and Planetary Sciences, University of California, Riverside, Riverside, CA, USA

Abstract The Wyoming Craton underwent tectonic modifications during the Laramide Orogeny, which resulted in a series of basement-cored uplifts that built the modern-day Rockies. The easternmost surface expression of this orogeny - the Black Hills in South Dakota - is separated from the main trend of the Rocky Mountains by the southern half of the Powder River Basin, which we refer to as the Thunder Basin. Seismic tomography studies reveal a high-velocity anomaly which extends to a depth of ~300 km below the basin and may represent a lithospheric keel. We constrain seismic attenuation to investigate the hypothesis that variations in lithospheric thickness resulted in the localization of stress and therefore deformation. We utilize data from the CIELO seismic array, a linear array that extends from east of the Black Hills across the Thunder Basin and westward into the Owl Creek Mountains, the BASE FlexArray deployment centered on the Bighorn Mountains, and the EarthScope Transportable Array. We analyze seismograms from deep teleseismic events and compare waveforms in the time-domain to characterize lateral variations in attenuation. Bayesian inversion results reveal high attenuation in the Black Hills and Bighorn Mountains and low attenuation in the Thunder and Bighorn Basins. Scattering is rejected as a confounding factor because of a strong anticorrelation between attenuation and the amplitude of *P* wave codas. The results support the hypothesis that lateral variations in lithospheric strength, as evidenced by our seismic attenuation measurements, played an important role in the localization of deformation and orogenesis during the Laramide Orogeny.

1. Introduction

Cratons, the cores of continents, typically resist tectonic deformation and are generally devoid of contemporary seismic and magmatic activity (e.g., Lee et al., 2011). Nevertheless, geophysical and geological observations indicate that cratons can be subject to the destructive effects of tectonic and mantle dynamics. Examples of this include the North China Craton (e.g., Gao et al., 2004; Kusky & Li, 2003; Zhu et al., 2012), the Dharwar Craton (Griffin et al., 2009), and the Brazilian Shield (Beck & Zandt, 2002; Kusky et al., 2014; Ramos et al., 1986). The circumstances that enable intracratonic deformation are debated, including the loss of their lithospheric keel caused by gravitational instabilities or convection (e.g., Conrad & Molnar, 1997; Huang et al., 2003), the rheological weakening of cratonic mantle due to rehydration (e.g., Humphreys et al., 2003), and other scenarios where the lithospheric mantle is modified.

The Wyoming Craton remained relatively immune to modification until its recent reactivation, which refers to the lithospheric thinning associated with the change of tectonic environment (Wang et al., 2013). After formation by the cratonization of Neoarchean volcanic arcs (Mueller & Frost, 2006) and accretion to the core of the North American Shield at ~1.8 Ga (Whitmeyer & Karlstrom, 2007), the craton experienced a long period of quiescence which ended with the onset of the Laramide Orogeny at 80 Ma. At that time, the shallow subduction of the Farallon Plate resulted in strong horizontal stress on the Wyoming Craton, causing the contraction of the crust by 50–60 km through a series of deep-seated, basement involved thrust faults (Axen et al., 2018; Bird, 1998; Coney & Reynolds, 1977; DeCelles et al., 1991; Dickinson & Snyder, 1978; Fan & Carrapa, 2014; E. D. Humphreys et al., 2015; W.T. Jackson et al., 2019; Saleeby, 2003). The orogeny uplifted widespread foreland arch systems, including the Bighorn Mountains and the Black Hills. The southern portion of the relatively flat Powder River Basin extends between these two ranges. To avoid confusion with the greater Powder River Basin, we refer to this southern extension as the Thunder Basin after the National Grassland of that name which occupies the area. Similar to the Black Hills–Thunder Basin pair, the Bighorn

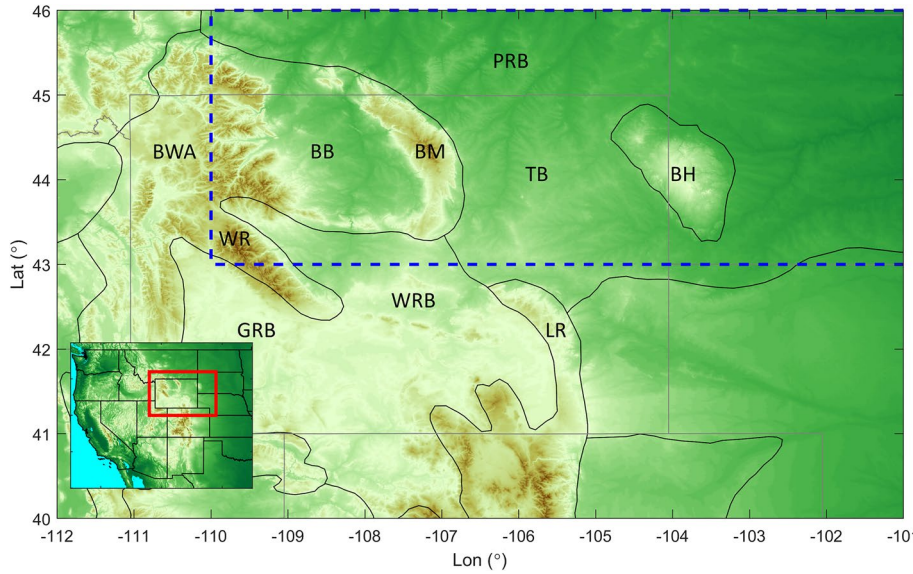

Figure 1. Physiographic provinces of the Rocky Mountains Front in the region surrounding the State of Wyoming (BB: Bighorn Basin, BH: Black Hills, BM: Bighorn Mountains, BWA: Beartooth-Washakie-Absaroka Ranges, GRB: Green River Basin, LR: Laramie Range, PRB: Powder River Basin, TB: Thunder Basin, WR: Wind River Range, WRB: Wind River Basin) are shown by black lines. Dashed blue rectangle marks the region where relatively dense seismic arrays are present and is the range in several subsequent figures. Gray lines are US state borders, and are also shown in several subsequent figures.

Mountains are flanked to the west by Bighorn Basin. This pattern of intermittent landforms composes much of the Rocky Mountains: discrete basement-cored uplifts away from the plate boundary, and has come to be known as Laramide Style deformation (Figure 1).

Important questions are still debated as to how Laramide style deformation proceeds: Why do uplifts occur in regions far inside the continent rather than close to the plate boundary? How is stress transferred among blocks and localized in certain regions? Is the variation of topography related to just to the strength of the crust or to the strength of the whole lithosphere? Do pre-existing structures influence these basement-cored uplifts?

Since the Wyoming Craton is large compared to the size of the mountain ranges contained within it, these problems have been approached from a variety of perspectives and scales. Receiver function (Yeck et al., 2014) and active source seismology studies (Worthington et al., 2016) suggest that pre-existing crustal heterogeneities or Moho topography resulted in the nucleation of foreland arches. Other interpretations, including "pure shear thickening" (Egan & Urquhart, 1993) suggesting the thickening of crust during orogeny and "lithospheric buckling" (Tikoff & Maxson, 2001) implying orogeny is associated with the folding of the entire lithosphere, have been introduced to interpret the formation of Laramide Style deformation. Passive-source seismic imaging reveals a NE-trending high-velocity anomaly extending from the Moho to ~300 km depth directly below the Thunder Basin (Dave & Li, 2016; Schmandt & Humphreys, 2010; Schmandt & Lin, 2014; Shen & Ritzwoller, 2016; Wang et al., 2016). We refer to this high-velocity anomaly as the Thunder Basin Block (TBB). The TBB's anomalous velocity structure has been interpreted in several ways: Wang et al. (2016) proposed the possibility that TBB is a remnant fragment of the ancient Farallon slab; Dave and Li (2016) suggested that the high-velocity anomaly may be a delaminating lithospheric keel, resulting from small scale convection caused by the shallow-angle subduction of the Farallon plate and the nearby Yellowstone Hotspot. In contrast, Humphreys et al. (2015) argue that the anomaly is evidence of ongoing recratonization by underplating the thinned lithosphere of the Wyoming Craton with the lithospheric mantle of a subducted oceanic plateau. These scenarios imply different rheological conditions beneath the Thunder Basin.

In this study, we characterize seismic attenuation in the eastern half of the Wyoming Craton and use our observations to better understand the relationship between lithospheric strength and Laramide style deformation. Observations of seismic attenuation may help to differentiate between the different hypotheses due to an integrated sensitivity to the lithosphere-asthenosphere system above a depth a of ~220 km (Soto Castaneda et al., 2021). We would expect an intact cratonic lithosphere to demonstrate universally low attenuation, while other cases may lead to either large or small variations in attenuation depending on the thickness of the strong lithosphere block. We show results that suggest the uplifted ranges of the Wyoming Craton are causally related to variations in lithospheric strength and thickness: regions with mountain ranges are characterized by high attenuation while nearby basins are characterized by low attenuation. From this perspective, Laramide style deformation may be a result of lateral stress transfer among pre-existing lithospheric blocks with distinct thickness and strength.

2. Data and Methods

2.1. Why Attenuation?

Although the processes that control seismic attenuation are debated, seismic attenuation can provide a constraint on lithospheric strength independent from constraints on seismic velocity (Jackson & Faul, 2010; Karato, 2008). This dissipation of seismic energy is quantified by the parameter t*, which represents the integrated effect of attenuation over the entire raypath:

$$t^* = \int \frac{dt}{Q(t)} = \int \frac{dx}{c(x)Q(x)}$$

where Q is the quality factor, and c is the seismic wave velocity. A perfectly elastic material has infinite quality factor. While measuring t* directly requires detailed knowledge of the source, the difference in t* for phases from the same source along different raypaths (Δt*) can be readily estimated. Since we measure the path-integrated attenuation, we have no direct constraint on where along the ray attenuation occurred, and the relative scarcity of data in the teleseismic case typically precludes a tomographic approach. However, given the very large difference in Q between the lithosphere and the low-viscosity asthenosphere (e.g., Dziewonski & Anderson, 1981; Montagner & Kennett, 1996) we assume the variations in t* stem from the differences in lithospheric thickness among regions: Lower t* values (negative Δt*) suggest thicker and stronger lithosphere blocks compared to regions with higher t* (positive Δt*). This assumption is in line with recent results from Alaska (Soto Castaneda et al., 2021) and northern China (Liu et al., 2021) which show that teleseismic attenuation measurements are most sensitive to structure below the crust and above ~220 km depth.

2.2. Data

To gain a better understanding of variations in lithospheric strength between the Black Hills, the Thunder Basin, and surrounding areas, we deployed a line of 24 broadband seismic stations spanning the region, that we refer to as the CIELO (Crust-Lithosphere Investigation of the Easternmost Expression of the Laramide Orogeny) array (Figure 2). Along with existing data from the EarthScope Transportable Array (TA) and the Bighorn Arch Seismic Experiment (BASE, Sheehan et al., 2009) which covers the NW corner of our study area, we are able to collect ~2000 P wave arrivals on the vertical channel from 48 deep events (hypocenter deeper than 250 km and magnitude greater than Mb 5.5, Figure 3). Seismic rays from deep events have the advantage that they only travel through the low-Q asthenosphere on the receiver side. The majority of our events come from the subduction zones located in Northeast Asia and South America, with a small number from Tonga and Western Europe (Figure 3), providing good back azimuthal coverage when compared to similar studies (Bezada, 2017; Byrnes et al., 2019).

2.3. Time Domain Measurement of Δt*

We adopt the time domain Δt* measurement method introduced in Bezada (2017) as it appears to be more robust with respect to confounding factors such as the scattering of seismic energy compared to the

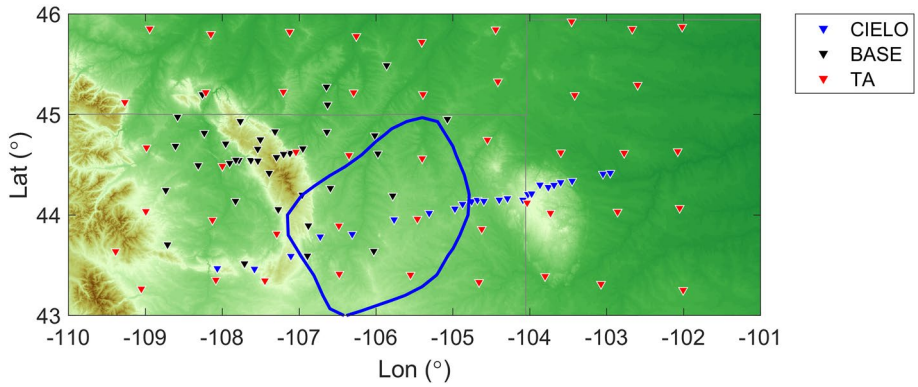

Figure 2. The location of seismic arrays in the region marked by blue dashed rectangles in Figure 1. Blue contour marks the boundary of a 2% high dVp anomaly in the velocity model of Schmandt and Lin (2014) at the depth of 200 km.

traditional spectral ratio method of Teng (1968) (Bezada et al., 2019; Byrnes et al., 2019). First, we produce an estimate of the unattenuated source seismic waveform for each event after filtering all traces with a band-pass filter of 0.02–3 Hz. We do this by selecting and stacking the seismic traces with the most impulsive first arrivals and the most high-frequency energy. We find Δt* for each recorded trace by comparing it with a numerically attenuated version of the source waveform estimate produced with the attenuation operator of Azimi (1968) in the frequency domain:

$$A = \exp\left\{-\omega\Delta t^{*}\cdot\left[\frac{1}{2}+\frac{i}{\pi}\ln\left(\frac{\omega}{\omega_0}\right)\right]\right\}$$

where only the the factor Δt^{*} has an impact on relative observations. We grid-search over Δt* values and choose the value that minimizes the L_2 norm of the misfit between the numerically attenuated source trace and the observed waveform in a selected window in the time domain. Results are culled by visually inspecting each best-fit attenuated waveform A demonstration of acceptance and rejection criteria can be found in Figure 4. In most cases, rejected measurements produce synthetic waveforms that are less well correlated with the observed waveform (e.g., Figure 4). However, the cut-off cross-correlation value was observed to vary from event to event and thus we prefer manual inspection to auto-selection as a means of quality-controlling the measurements. In this way, we obtained 1,489 Δt* measurements from 137 stations.

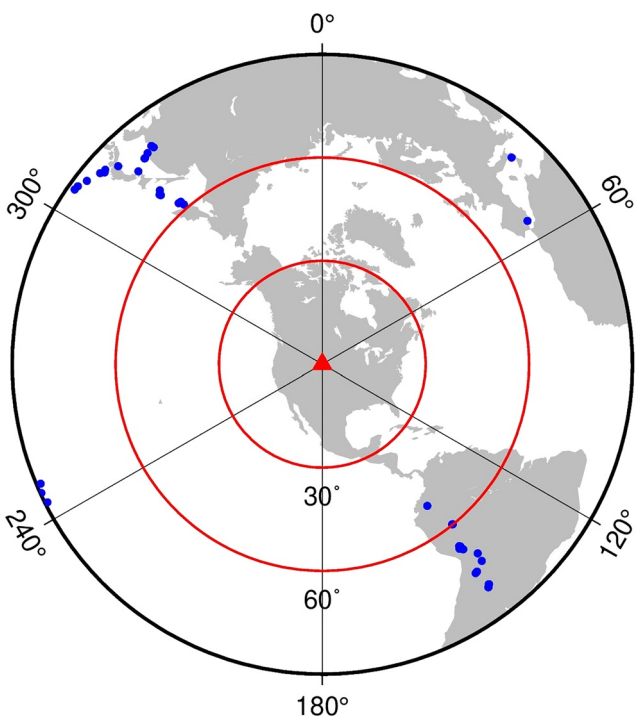

Figure 3. The deep events (depth ≥ 200 km, Mw ≥ 5.5) that are picked up by the seismic networks in our study.

2.4. Inversion Approach

Due to the limited number of available events and seismic waveforms, it is not feasible to constrain a 3D model for the entire region. Instead, we invert for a 2D (map-view) model of lateral variations in attenuation.

We use the Markov Chain Monte-Carlo (MCMC) approach described in Byrnes et al. (2019) to invert for a map of lateral variations in attenuation. A deterministic inversion for this type of data set (Bezada, 2017) requires subjective hyperparameters such as damping, smoothing, and station terms which have non-negligible impacts on the inverted model (Figures S1 and S2 in Supporting Information S1). Bayesian approaches based on MCMC offer a useful alternative that introduce minimal external constraints (e.g., Bodin et al., 2012; Malinverno & Briggs, 2004; Ravenzwaaij

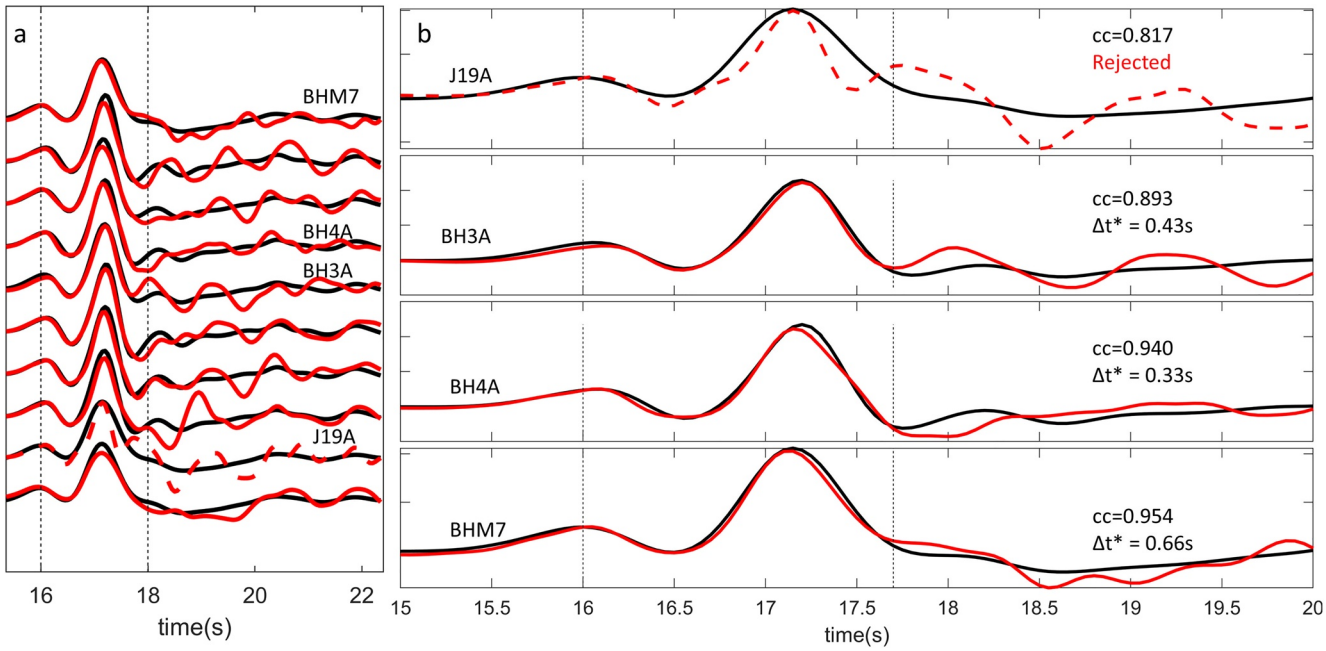

Figure 4. (a) Δt* measurement results for one of the events picked up by Transportable Array (TA) and Bighorn Arch Seismic Experiment array. (b) Waveform matching results for the stations marked in (a), where the traces plotted in red represent the synthetic data attenuated from the prototype source trace, and the black traces are the waveforms from the stations. The Δt* measurement on station TA.J19A is rejected due to the low correlation between the synthetic and observed data.

et al., 2014). At the beginning of the inversion, several independent chains are initialized with models described by a random number of nodes with stochastically generated Δt* values. Five possible manipulations to each model can occur, including (a) generating a new node; (b) removing an existing node; (c) changing the value of Δt* of a node; (d) moving an existing node to a different location; (e) perturbing the uncertainty of the data. Searching over the uncertainty of the data allows the inversion to perform well under high levels of noise, as is typically present in such studies, and is a primary motivation for using the MCMC approach (Bezada et al., 2019; Byrnes & Bezada, 2020; Byrnes et al., 2019). Since the starting model is randomly generated, we set an empirical "burn-in" stage during which we do not keep the generated models. After the overall misfit of the model decreases sufficiently during the burn-in period (Figure S3 in Supporting Information S1), we keep one out of every 100 models to reduce the redundancy of the model set. The number of chains and iterations have an impact on the overall results, but models generally agree with each other on the location and magnitude of anomalies (Figure S4 in Supporting Information S1). Based on several trial inversions (Figure S5 in Supporting Information S1), we choose to perform 10^6 iterations over 30 chains.

2.5. Scattering Observations

As discussed above, more attenuated seismic waveforms appear broader since high-frequency energy has been absorbed by the propagating medium. Unfortunately, other wave propagation phenomena can mimic this effect on the waveform. In particular, the scattering of seismic energy off small-scale heterogeneities may alter the seismic wavefield by delaying the arrival of high frequency seismic energy. Possibly, then, the apparent attenuation of the waveforms in our study could be an artifact caused by scattering. For example, Cafferky and Schmandt (2015) pointed out that the scattering of energy from dipping interfaces may exaggerate the Δt* variations measured by the frequency domain method, as indicated by the presence of a significant amount of high-frequency energy on the transverse component.

Given these considerations, we make an additional measurement described in Bezada (2017) to quantify the scattering of seismic energy at each station. The strength of the high-frequency coda in the waveforms is measured by what we refer to as the Scatter Index (SI), which quantifies the amount of high-frequency energy in the coda. The seismic coda in the vertical channel that lies in a fixed length window after the P

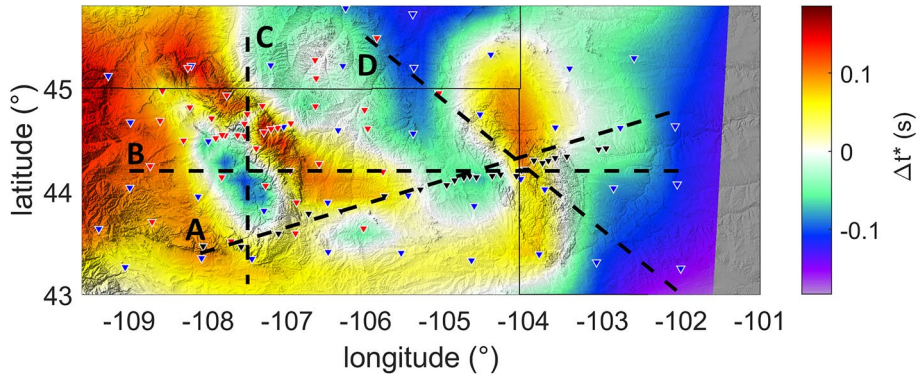

Figure 5. The preferred Markov Chain Monte-Carlo inversion result ensemble with 30 chains and 1e6 iterations on each chain. The Δt* is shown in color overlaid on the shaded relief topography (Etopo1). Triangles mark the locations of seismic stations: blue: TA stations; red: BASE stations; black: CIELO stations. Dashed lines indicate the locations of cross-sectional plots shown in Figure 7.

arrival is high-pass filtered with various corner frequencies (Figure S6 in Supporting Information S1). These measurements are sensitive to the wavelength of the scatterers, with SI measured at higher frequency likely correlated with scattering effects at shallower depths. We set the window to be 10 s in length and 5 s after the P arrival because that is the typical location of the coda for the events used here and window size seems to have minor impact on SI measurements (Figure S7 in Supporting Information S1). The index is computed as the ratio between the envelopes of filtered and unfiltered traces; to reduce the influence of noise, we subtract the envelope of data in a 10 s window 5 s before the P arrival. We only retain SI measurements for traces with a high signal to noise ratio (SNR > 5). More details on the SI calculation are given in the Supplementary Information. Larger index values reflect more high-frequency energy transferred to the P wave coda. To demonstrate the distribution of scattering magnitude, we demean the measurements by events and invert with the same MCMC approach as used for the attenuation observations. Since higher frequency filters lead to fewer traces with high SNR, we focus on the results filtered with 1, 2 and 4 Hz high-pass filters.

3. Results

Figure 5 shows the mean of the ensemble models for Δt*. To first order, regions that are considered to be part of the interior of Laurentia (the northern and eastern parts of the study area) show overall low Δt*, as much as −0.15 s, indicating regionally weak attenuation. In contrast, the main trend of the Rocky Mountains lying in the west end of the study area shows high Δt* (~0.2s) values, indicating strong attenuation. The Wyoming Craton does not demonstrate universally high or low Δt* values: basins (such as the Thunder Basin (TB) and Bighorn Basin (BB)) display low Δt* (approximately −0.1s) and the highest Δt* (0.1–0.2s) are clustered around the mountain ranges (Bighorn Mountains (BM), Wind River Ranges (WR), and the Black Hills (BH)).

Our analysis of potential confounding factors leads us to conclude that the Δt* model primarily reflects intrinsic attenuation. The Δt* variation positively correlates with topography in the region (correlation coefficient of 0.61, Figure S8 in Supporting Information S1). On the other hand, our models of SI (Figure 6) all demonstrate strong to moderate level of anti-correlation with Δt* results (4 Hz: −0.60, 2 Hz: −0.51, 1 Hz: −0.50, Figure S9 in Supporting Information S1). In particular, regions with higher Δt* values coincide with low scattering index (e.g., the Bighorn Mountains, the Beartooth-Washakie-Absaroka Ranges, Figure 5), indicating the high frequency energy was absorbed rather than scattered. Although it has been suggested that mountain ranges may lead to stronger crustal scattering effects due to the prevalence of dipping surfaces (Cafferky & Schmandt, 2015), we do not observe this. The gradient magnitude of the topography (Text S1 and Figure S10b in Supporting Information S1) and terrain roughness (Riley et al., 1999) (Figure S10d in Supporting Information S1) both show weak correlations with the scattering index (2 Hz model, correlation coefficient: −0.28, −0.2 respectively), implying the topography is not a major driver of scattering in this region. These results suggest that extrinsic attenuation due to scattering or topography effects is unlikely to

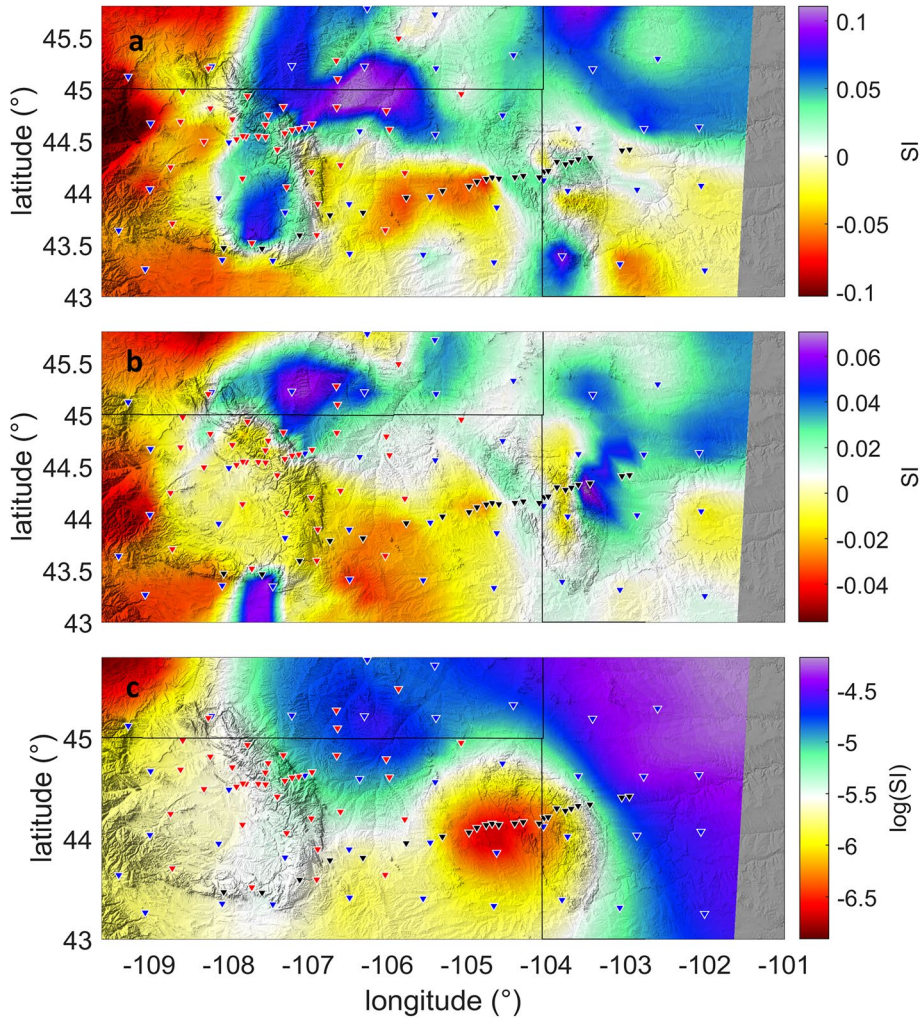

Figure 6. Scatter Index models inverted with measurements under different frequency bands (a) >1 Hz, (b) >2 Hz, (c) >4 Hz). Note that colorbar is reversed from the attenuation maps, and thus similarities between SI and attenuation maps indicate anticorrelation between the two.

be the first-order driver of the observed lateral variations in Δt*, though we cannot reject some contribution from variations in the strength of scattering. It has also been suggested that an as-yet unidentified wave propagation phenomenon may lead to artificially low Δt* within basins (Soto Castaneda et al., 2021), and we do indeed observe low Δt* in basins in this study. We note, however, that previous results show that our methodology for measuring Δt* does not universally assign high values to mountainous regions and low values to basins. Byrnes and Bezada (2020) observed a high Δt* anomaly in the Salton Trough, a low-lying and flat basin, while Deng et al. (2021) observed a local minimum in Δt* in the rugged mountainous ranges of the Chuan-Dian Block in southwestern China.

In addition, the ensemble Δt* model has an overall low uncertainty (~0.06s) relative to the magnitude of the anomalies (Figure S11a in Supporting Information S1). Where stations are more densely distributed, the standard deviations typically fall to approximately 0.04s, while uncertainties tend to be higher near the boundary of distinct Δt* anomalies (~0.08s). A detailed look at the Δt* distribution among different models can be found in Figure S11b in Supporting Information S1, where the mean of the ensemble models fits well with the estimates with highest probability, consistent with the absence of significant skew in the distributions.

As a check on the Bayesian model, we also invert the quality-controlled data with the linear inversion approach (Bezada, 2017, Figure S2 in Supporting Information S1). We choose the hyperparameters based on

the tradeoff between model norm and misfit to the data. The outline and magnitude of Δt* anomalies in the Bayesian model and our preferred linear inversion are highly similar (Figures S2 and S4 in Supporting Information S1) and would lead to the same general conclusions. We choose the Bayesian model as our preferred model because it more adequately handles observation uncertainty, which it determines to be ∼0.15 s.

The uncertainty in the data may reflect a random component in the measurement, or be related to systematic differences between different subsets of events. We explore subsets of events in Figure 8. We produce two models, Kurils Model (KM) and South America Model (SAM), by inverting data from the Kurils (14 events) and South America (10 events), respectively. While KM and SAM show a similar trend of Δt* (high to low from west to east), the magnitude of Δt* at the TBB in the KM (∼0s) is much smaller than that of SAM (∼−0.1s). The reason behind this difference may be the attenuation in the deeper Earth sampled differently by the raypaths, since the backazimuth of the event sets vary drastically. However, the CIELO deployment better recorded events from South America than from the Kurils around the Black Hills, and so the the difference on the western edge of the Black Hills may be related to the availabibilty of the data (Tables S1, S2, and Figure S12 in Supporting Information S1). Nevertheless, the overall pattern of Δt* is consistent with our preferred model and neither subset would lead to substantially different general interpretations, with the possible exception of better constraints from SAM confirming the weakened anomaly on the western edge of the Black Hills.

4. Discussion

4.1. Overall Variation of Δt*

Lateral variations in attenuation likely reflect variations in the thickness of the lithosphere or the quality factor of the asthenosphere because of the contrast in Q of the lithosphere and asthenosphere in 1D Earth models (Dziewonski & Anderson, 1981; Montagner & Kennett, 1996; Romanowicz & Dziewonski, 2010). Our observation of the transition of Δt* from west to east agrees well with existing Δt* models (Cafferky & Schmandt, 2015), global and regional Q models (Bao et al., 2016; Dalton et al., 2008), LAB depth transition implied by observations of heat flow (Blackwell et al., 2011) and seismic velocity models (e.g., Porter et al., 2016; Schmandt & Lin, 2014; Shen & Ritzwoller, 2016; Xie et al., 2018). The most tectonically active regions of the study area, primarily in the Rocky Mountains, feature higher Δt* values, which agrees with the expectation of thinned lithosphere in these areas following the flat subduction of the Farallon Slab (e.g., DeCelles, 2004; Dickinson & Snyder, 1978). The Great Plains, on the contrary, have remained largely stable since the Precambrian, and so do the low Δt* values here again conform to expectation. Superimposed on this general west-to-east pattern are considerable fluctuations in Δt* of 0.1–0.25 s, mostly within the Wyoming Craton, which agrees with the fact that the Wyoming Craton is not underlain by universally high seismic velocities. The Laramide style deformation that the Wyoming Craton experienced is characterized by discrete, narrow ranges separated by basins (Mueller & Frost, 2006) and, interestingly, the Δt* fluctuations within the Wyoming Craton correlate well with these features. Below, we explore these correlations, focusing on the regions associated with the Black Hills and the Bighorn Arch.

4.2. The Thunder Basin and the Black Hills

Of all the Laramide ranges, the Black Hills are the most isolated from the main trend of the Rocky Mountains; separated by the undeformed region we are referring to as the Thunder Basin. Although the eastern margin of the Wyoming Craton is under debate (the Black Hills, according to Mueller and Frost (2006); or the Bighorn Mountains, according to Kilian et al., 2016 and Worthington et al., 2016), the general consensus is that the Black Hills are a basement cored uplift like those prevalent in the Rocky Mountains. The Black Hills were uplifted at about 62 Ma (Lisenbee et al., 1993) with several phases of magmatism following until 39 Ma (Kirchner, 1977). Like other Laramide-associated uplifts, the Black Hills feature a high gravity anomaly (Simpson et al., 1986) which could be related to crustal shortening or older basement structures. In contrast, the TBB remained undeformed during the Laramide Orogeny. Notably, available seismic velocity models (Schmandt & Lin, 2014, SL14; Shen & Ritzwoller, 2016, SR16) reveal a contrast between the two blocks (Figures 7a–7d). High velocities beneath the TBB extend to depths greater than 300 km (Humphreys et al., 2015), while the Black Hills sit directly above a low-velocity anomaly. The nature of the TBB is

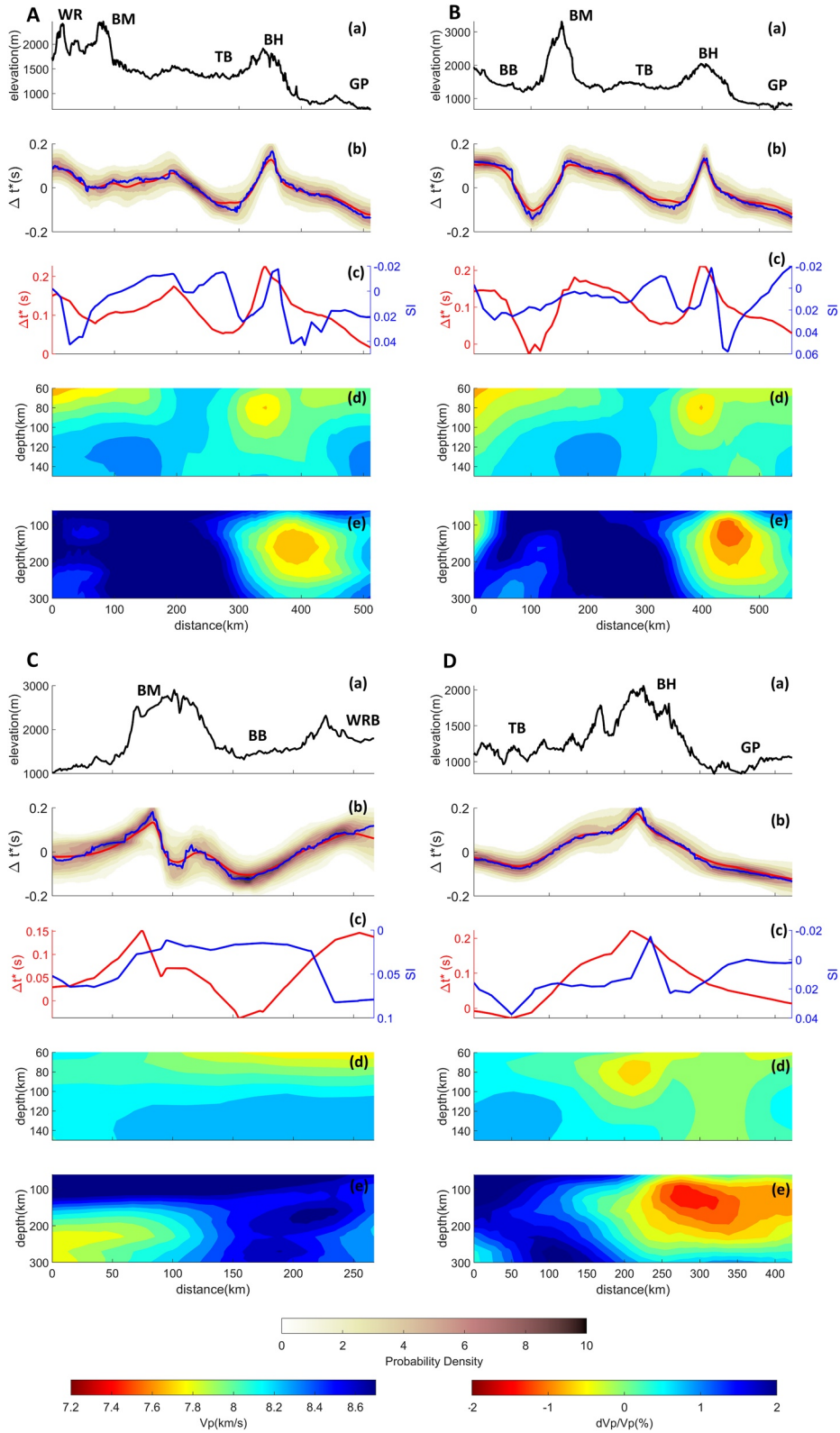

Figure 7. (a) Elevation, (b) Δt* probability distribution along with mean (red) and mode (blue), (c) Detrended Scattering Index (>2 Hz) and detrended Δt* (note that the *Y* axis of the scatter index plot is inverted to facilitate comparison with Δt*), (d) Vp model (SL14), (e) dVp/Vp model (SR16) along the cross-sectional lines shown in Figure 5.

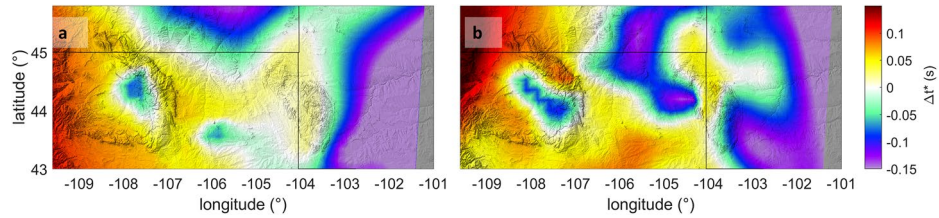

Figure 8. Comparison of Markov Chain Monte-Carlo inversion results using only part of the measurements: (a) the inversion result (KM) only using events from Kuril region (b) the inversion result (SAM) only using events from South America.

under debate: popular interpretations include the downwelling remnants of the Wyoming Craton (Dave & Li, 2016), a remnant of Farallon lithosphere (Wang et al., 2016), and the depleted lithosphere of the Shatsky conjugate (Humphreys et al., 2015). Regardless, these models would all suggest that the lithosphere associated with the Thunder Basin is thicker than that beneath the Black Hills.

In agreement with the velocity models, Δt* is lower in TBB than in BH and the contrast between the two regions (~0.15s) greatly exceeds model uncertainty. In Section 3 we introduce the SI and show that it does not generally support scattering as the main cause of the observations that we interpret as intrinsic attenuation. To further explore the relationship between SI and Δt* at shorter wavelengths comparable to the scale of basins and mountain ranges, we remove the longest-wavelength variations by fitting a plane to each model (the detrended maps are shown in Figure S13 in Supporting Information S1 and the profiles through the detrended models are in the "c" panels of Figure 7). The anti-correlation of these two independent measurements is evident over line A, line B and line D: BH generally coincide with a local maximum in Δt* and a local minimum in SI (>2 Hz). Although SI fluctuates more strongly around TBB, the eastern half demonstrates opposite trend compared to Δt*. Therefore, if SI (>2 Hz) is a good indicator of scattering effects of teleseismic P waves, this pattern suggests the Δt* contrast between TBB and BH is underestimated.

The observed Δt* variation cannot result solely from variations in sediments or the crust. The TBB is covered by a sedimentary basin, while crystalline basement outcrops in the BH (Shah & Boyd, 2018), so the attenuating sediments would produce the opposite of our observed pattern. Moreover, given that the thickness of the sedimentary layer (~3 km to the basement for this region) (Shah & Boyd, 2018) is almost negligible compared to that of the highly attenuating asthenosphere and is shorter than the dominant teleseismic wavelength, Δt* variation due to sediments should be negligible. Concerning the bulk crust, ongoing exhumation in the mountains would lead to heat advection and consequently higher crustal temperatures and lower Q values than in the adjacent basin (Reiners & Brandon, 2006). Although available Lg attenuation models for the contiguous US (Gallegos et al., 2014, 2017) display little variation among the two blocks, it could be argued that those studies lacked the necessary resolution to show the difference. Hence, we test if intrinsic properties of the crust or the ongoing exhumation of the crust could contribute to the signal.

We estimate the maximum Δt* variation that could be generated by differences in crustal Q as documented in the Lg models with a simple block model outlined in Figure 9a. The Δt* is computed over a range of $\boldsymbol{Q}_{low}$, quality factor in the more attenuating crustal block, and crustal thickness h. For simplicity, we assume that $\boldsymbol{Q}_p = 2.25\boldsymbol{Q}_s$ (Karato & Spetzler, 1990). Although lower $\boldsymbol{Q}_p/\boldsymbol{Q}_s$ is possible and observed in tectonic settings different from that of our study area (e.g., Wei & Wiens, 2020), we use the higher ratio to consider the maximum Δt* contrast that could originate from crustal Q variations. We also assume a moderate frequency dependency factor ($\alpha = 0.3$) to convert Q estimates performed at other frequencies to 1 Hz. As shown in Figure 9a, even if $\boldsymbol{Q}_p$ is as low as 100 and the crustal thickness is 50 km, we can only generate ~0.05s of Δt*. Such a low quality factor for the crust is uncommon (Toksöz et al., 1988), and so we conclude that extreme values can only explain a small fraction of the signal. This implies that even if the exhumation-driven heat advection made crustal Q in the mountains as low as anywhere else in the US, this crustal Q contrast would not significantly contribute to our observations. Furthermore, although the temperature curves under different erosion rates modeled by Reiners and Brandon (2006) vary in the crust, the maximum temperature is always below 600 C°. At these temperatures, Qp of rocks is expected to be above 1,000 according to all current models for anelasticity (Havlin et al., 2021). Hence, the contribution to Δt* from the crust given above

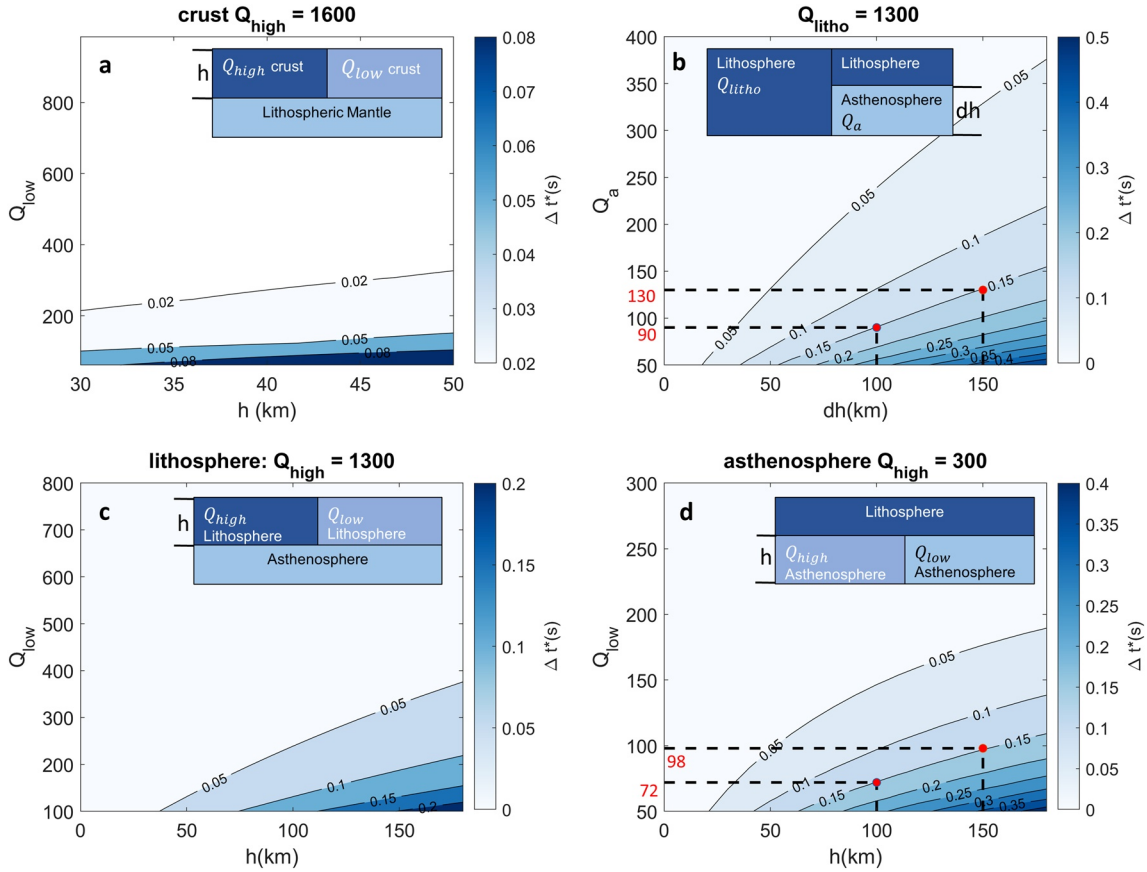

Figure 9. Estimation of Q_p and column thickness under multiple scenarios: (a) h is the thickness of crust, Q_{high} is fixed to be 1,600; for each Q_{low} and h pair, we compute how much Δt* can be generated; (b) dh is the variation of lithosphere thickness between two column; Q_a is the Q of underlying asthenosphere; for each dh and Q_a pair, the corresponding Δt* is computed. (c) Similar to (a) except that here h is the thickness of the lithosphere, Q_{high} is fixed to be 1,300; (d) similar to (a) except that here h represents the thickness of asthenosphere with Q variation. In all cases, Vp of the high Q block is assumed to be 7 km/s and the Vp of low Q block is set to be 10% (case (a)), 2% (case (b) and (c)), 0% (case (d)) slower, respectively.

is likely to be an overestimate. If we extrapolate the influence of exhumation on temperature over the entire mantle lithosphere (Figure S14 and Text S2 in Supporting Information S1), under very extreme erosion rates (5 km/Myr) the elevated temperatures add 0.03s of Δt*. Since this erosion rate is substantially larger than the estimated erosion rate in the valleys around the Black Hills (~200 m/Myr, Small & Anderson, 1998), we ultimately reject crustal processes as the origin of the difference in attenuation.

Since variations in in lithospheric thickness in the region are well established, we next consider the case of varying lithospheric thickness as a possible explanation for the Δt* contrast. We assume the lithosphere's $\boldsymbol{Q_p}$ to be 1,300 following PREM and QL6 (Durek & Ekström, 1996; Dziewonski & Anderson, 1981), and we compute the corresponding Δt* for a range of $\boldsymbol{Q_p}$ in the asthenosphere ($\boldsymbol{Q_a}$) and the difference in thickness between the two lithospheric columns (***dh***). Again the frequency dependence is set to be moderate ($\alpha = 0.3$) in the absorption band and the Q_p/Q_s ratio is set to 2.25 to reflect the general case of weak bulk attenuation. The results are presented in Figure 9b and show that 0.15s of Δt* can be reached for a range of ***dh*** and $\boldsymbol{Q_a}$ pairs. For instance, when ***dh*** is 150 km, we need a $\boldsymbol{Q_a}$ at ~130, which is a typical value of Q for asthenosphere at 200 km depth from the PREM model; if ***dh*** is 100 km, then $\boldsymbol{Q_a}$ has to be ~90, which suggests the presence of melt or premelt conditions according to lab experiments, extrapolation calculations and seismic observations at dominant frequency of 1 Hz (e.g., Abers et al., 2014; Jackson & Faul, 2010; Takei, 2017). Differentiating between these scenarios is beyond the scope of this study, but this calculation shows that the difference in Δt* between the TBB and BH is consistent with a variation in the thickness of the lithosphere of ~100 km. Additional observations such as heat flow (Blackwell et al., 2011) and seismic velocity tomography (Schmandt & Lin, 2014; Shen & Ritzwoller, 2016) indicate the Black Hills mark a region of low

seismic velocities. The TBB velocity anomaly extends to a depth of ~300 km and the slow velocity anomaly (~1%–~3%) beneath the BH extends from depths of 70–300 km. This is consistent with the calculation above that can explain the change in Δt* between the two blocks. A corollary would be that the Black Hills may sit above a weaker and more attenuating zone of the lithosphere, while the surrounding lithosphere is thicker and less attenuating.

4.3. The Bighorn Basin and Bighorn Mountains

The uplifting of the Bighorn Mountains was analogous in many ways to the uplifting of the Black Hills–the Bighorns were raised during the Laramide Orogeny on the eastern edge of a relatively undeformed basin, the Bighorn Basin (Erslev, 2005). In Figures 7a and 7c, our model shows that the Bighorn Basin features a local minimum in Δt* (~−0.1s) while the Bighorn Mountains display a local maximum in Δt* (~0.1s), marking one of the largest contrasts between neighboring geological units in the map and in clear concordance with the pattern observed at the Black Hills. Contrary to the Black Hills, however, neither currently available tomographic models nor heat flow studies imply elevated temperatures or thinned lithosphere beneath the Bighorn Mountains. Although the northern section of the Bighorn Mountains sits above a 0.5% slow $\boldsymbol{v}_p$ anomaly at ~200 km (Figure 7c), this anomaly does not extend under the entire mountain range and is missing from the west-east cross-section of Figure 7b (Shen & Ritzwoller, 2016). SL14 should be able to resolve structures with the scale of the Bighorn Mountains (~50 km from west to east), nevertheless, the selection of smoothing parameters seems to be biased toward larger scale anomalies.

In addition to seismic velocity models, we also consider other observations that may suggest the source of Δt* differences. As discussed in the previous sub-section, the Δt* contrast in the Bighorn Mountains cannot be explained by fluctuations in sediment thickness (Shah & Boyd, 2018), nor are variations in crustal Q sufficient to generate such large Δt*. A possible model of Lg attenuation (Gallegos et al., 2017) does imply sufficient variation in Q between the basin and mountains (0.5 Hz, 400 to 100, respectively), but large disagreements between models constructed with different frequencies implies that scattering produces this contrast (Gallegos et al., 2017). Therefore, we consider several possible scenarios: Δt* contrast caused by (a) $\boldsymbol{Q}_p$ variation within the lithosphere (Figure 9c); (b) $\boldsymbol{Q}_p$ variation within the asthenosphere (Figure 9d) (c) variations in lithosphere thickness (Figure 9b). The method is similar to that presented in Section 4.2, where we perturb the range of Q variations and layer thickness. For case 1, it is not likely that the variations in $\boldsymbol{Q}_{low}$ and lithospheric thickness can lead to ~0.15 s difference in Δt*. For case 2, under certain scenarios (e.g., $\boldsymbol{Q}_{low}$ of 72 and layer thickness of 100 km), 0.15s of Δt* can be explained. Although these values are compatible with geophysical observations (Pozgay et al., 2009; Rychert et al., 2008), the presence of melt is expected for these quality factors (Abers et al., 2014), so a process for the local production of melt within the Wyoming Craton would be needed. However, no other evidence suggests the presence of melt in this region, because (a) the Bighorn domain experienced limited magmatism prior and post Laramide (Reiners & Farley, 2001); (b) in regions of a similar setting associated with the presence of melt, such as the central Appalachian Mountains, volcanic outcrops (Mazza et al., 2014), extremely high conductivity (Evans et al., 2019) and larger Δt* contrast (~0.26 s, Byrnes et al., 2019) have been observed. Case 3 appears simpler and is consistent with the discussion in Section 4.1, suggesting only a thicker lithosphere underneath the Bighorn Basin. While the lithosphere can in principle vary in both thickness and $\boldsymbol{Q}_p$, Figure 9 shows that the thickness of lithosphere has a larger impact.

4.4. Implications for Laramide-Style Deformation

Motivated by the above observations and analyses, we speculate that the the interspersed mountains and basins characteristic of Laramide-Style deformation reflect variations in the strength of the lithosphere, which are in turn reflected in Δt*. Rheological heterogeneities in the lithosphere would, in this view, play a major role in the localization of deformation: the contracting stress produced by the subducting slab would be localized in the regions where the lithosphere is weak and thin, while thicker and therefore stronger blocks would have resisted deformation and transferred the stress laterally. The hypothesis is supported by the evident correlation between topography, Δt*, and seismic velocity structure in the region of the Black Hills and the Thunder Basin. Due to the sensitivity of Δt* measurements to the structures above a depth of

220 km (Liu et al., 2021; Soto Castaneda et al., 2021), variations in Δt* are likely due to variations in lithospheric thickness between the different blocks (i.e., Figure 9).

Variations in the thickness of mantle lithosphere is a distinct mechanism from the typically discussed mechanisms for the localization of deformation in this region. Previous studies have typically associated Laramide uplifts with pre-existing crustal weaknesses (Erslev & Koenig, 2009), which primarily manifest as faults and undulations in the depth of the Moho as revealed by receiver functions (Worthington et al., 2016; Yeck et al., 2014). Yeck et al. (2014) in particular gives several hypothetical scenarios, including: (a) the detachment of the crust to the lithospheric mantle under shortening stress, (b) the nucleation of deformation over the preexisting Moho geometry prior to the Laramide Orogeny, (c) the buckling of the entire lithospheric system during compression. These scenarios are not incompatible with our observations, though our Δt* results cannot be explained by crustal structure alone. Possibly, prior variations in lithospheric strength contributed to the different response to shortening stress in all these paradigms, such as in a scenario where the crustal-scale weaknesses develop in response to variations in the strength of the mantle lithosphere. The causation is unlikely to run in the opposite direction, where the lithosphere was thinned near zones of crustal weakness. We also note that models that imply lithospheric thickening during shortening, such as the "pure-shear thickening" hypothesis (Egan & Urquhart, 1993), predict the opposite correlation between Δt* and topography that we observe, and therefore can be rejected. The exception would be if this thickening led to lithospheric delamination and ultimate thinning. In that case, we may expect similar Δt* pattern, but the scenario is less likely considering the small amount of shortening (∼20 km) at the Black Hills during the Laramide Orogeny (Singleton et al., 2019) and the large contrast in lithosphere thickness compared to TBB.

Our results also speak to the debate on the nature of TBB. The overlap between high velocity anomalies and low Δt* suggest the TBB is strong and thick, and so more likely to reflect intact lithosphere than an actively delaminating root. In order to explain our results, the delaminating root would need to fill the area of the TBB where we observe low attenuation, instead of collapsing into a narrower column as in geodynamic simulations (e.g., Johnson et al., 2014; West et al., 2009). On the other hand, the recratonization model by Humphreys et al. (2015) cannot be ruled out with our observations, since both cratonic lithosphere and depleted oceanic lithosphere would appear as high-velocity, high-Q bodies. One caveat is that recratonization would have had to protect the overriding lithosphere from deformation immediately after, or even during emplacement of the allochthonous keel. This recratonization process, though, may not be necessary to account for the thick lithosphere present at TBB, considering the study area's proximity to the ancient Wyoming Craton. The hypothesis that deformation is localized in part by variations in the strength of the upper mantle predicts that this pattern of apparent attenuation could be extrapolated to much of the Rocky Mountains, where the Laramide style deformation is ubiquitous, and other areas showing Laramide-style deformation such as the Sierras Pampeanas (e.g., Ramos et al., 1986). Patterns of this sort have been observed with seismic attenuation in the Iberian Pennsiula (Bezada, 2017) and in Southern China (Deng et al., 2021) where basins have remained undeformed during diffuse deformation, but such a pattern has not to our knowledge been previously observed within a recent oregony. If pre-existing crustal structure alone can localize deformation, then one would not expect the observed correlation between uplift and lithospheric thickness in these regions. We speculate instead that in Laramide-style ranges the lithosphere beneath the basins should be generally thicker than beneath the surrounding mountains.

5. Conclusions

With time-domain analysis of teleseismic attenuation of first-arriving *P*-phases, we produce a model of Δt* in northern Wyoming and surrounding regions. The Δt* values generally decrease from west to east, which agrees well with previous Δt* studies for the region. Within the Wyoming Craton, we observe higher Δt* in the prominent mountain ranges (the Bighorn Mountains and the Black Hills) and lower Δt* in adjacent basins (the Bighorn and Thunder Basins, respectively). We conclude that the Δt* model primarily reflects variations of intrinsic attenuation in the lithosphere-asthenosphere system, since the results anti-correlate with a proxy for the scattering of the wavefield. We also observe a positive correlation between topography and Δt* with high confidence. In available seismic velocity models, the Black Hills and Thunder Basin are above slow and fast velocity anomalies, respectively, which agrees well with our results. We conclude that the lithosphere beneath the mountains is thinner than that beneath the basins. Considering the tectonic

environment and broader scale of deformation during the Laramide Orogeny, the result suggests the stress transferred by pre-existing stronger and thicker lithosphere blocks to weaker zones could have led to the formation of the Black Hills and the Bighorn Mountains. We speculate similar observations could be made in other Laramide ranges if there was sufficiently dense station coverage. We conclude that lateral variations in lithospheric strength and thickness, as evinced by our seismic attenuation measurements, played an important role in the localization of deformation and orogenesis during the Laramide Orogeny.

Data Availability Statement

The method and code used in this study has been open-sourced at https://github.com/jsbyrnes/tSToolbox (https://doi.org/10.5281/zenodo.4277716). The data set containing the seismic data and the corresponding Δt^* measurements is available at figshare data repository (https://doi.org/10.6084/m9.figshare.14794398). The data from BASE array can be accessed at the IRIS DMC (http://ds.iris.edu/mda/XV/?timewindow=2009-2010), and the data from CIELO array will be released no later than 2022-12-31.

Acknowledgments
This work was funded by the National Science Foundation (EAR-1944998, EAR-1827277), University of Minnesota (Proposal 325013), and University of California, Riverside (Regents Faculty Fellowship). We would like to thank Geoffrey Abers and one anonymous reviewer for their meticulous editing suggestions and Hanlin Liu for frequent discussion over this project.

References

Abers, G. A., Fischer, K. M., Hirth, G., Wiens, D. A., Plank, T., Holtzman, B. K., et al. (2014). Reconciling mantle attenuation-temperature relationships from seismology, petrology, and laboratory measurements. *Geochemistry, Geophysics, Geosystems*, *15*(9), 3521–3542. https://doi.org/10.1002/2014GC005444

Axen, G. J., van Wijk, J. W., & Currie, C. A. (2018). Basal continental mantle lithosphere displaced by flat-slab subduction. *Nature Geoscience*, *11*(12), 961–964. https://doi.org/10.1038/s41561-018-0263-9

Azimi, S. A. (1968). Impulse and transient characteristics of media with linear and quadratic absorption laws, Izvestiya. *Physics of the Solid Earth*, *2*, 88–93.

Bao, X., Dalton, C. A., Jin, G., Gaherty, J. B., & Shen, Y. (2016). Imaging Rayleigh wave attenuation with USArray. *Geophysical Journal International*, *206*(1), 241–259. https://doi.org/10.1093/gji/ggw151

Beck, S. L., & Zandt, G. (2002). The nature of orogenic crust in the central Andes. *Journal of Geophysical Research: Solid Earth*, *107*(B10), ESE 7-1–ESE 7-16. https://doi.org/10.1029/2000JB000124

Bezada, M. J. (2017). Insights into the lithospheric architecture of Iberia and Morocco from teleseismic body-wave attenuation. *Earth and Planetary Science Letters*, *478*, 14–26. https://doi.org/10.1016/j.epsl.2017.08.029

Bezada, M. J., Byrnes, J., & Eilon, Z. (2019). On the robustness of attenuation measurements on teleseismic P waves: Insights from micro-array analysis of the 2017 North Korean nuclear test. *Geophysical Journal International*, *218*(1), 573–585. https://doi.org/10.1093/gji/ggz169

Bird, P. (1998). Kinematic history of the Laramide orogeny in latitudes 35°–49°N, western United States. *Tectonics*, *17*(5), 780–801. https://doi.org/10.1029/98TC02698

Blackwell, D., Richards, M., Frone, Z., Batir, J., Ruzo, A., Dingwall, R., & Williams, M. (2011). *Temperature-at-depth maps for the conterminous US and geothermal resource estimates*. Southern Methodist University Geothermal Laboratory.

Bodin, T., Sambridge, M., Rawlinson, N., & Arroucau, P. (2012). Transdimensional tomography with unknown data noise: Transdimensional tomography. *Geophysical Journal International*, *189*(3), 1536–1556. https://doi.org/10.1111/j.1365-246X.2012.05414.x

Byrnes, J. S., & Bezada, M. (2020). Dynamic upwelling beneath the salton trough imaged with teleseismic attenuation tomography. *Journal of Geophysical Research: Solid Earth*, *125*(11), e2020JB020347. https://doi.org/10.1029/2020JB020347

Byrnes, J. S., Bezada, M., Long, M. D., & Benoit, M. H. (2019). Thin lithosphere beneath the central Appalachian Mountains: Constraints from seismic attenuation beneath the MAGIC array. *Earth and Planetary Science Letters*, *519*, 297–307. https://doi.org/10.1016/j.epsl.2019.04.045

Cafferky, S., & Schmandt, B. (2015). Teleseismic P wave spectra from USArray and implications for upper mantle attenuation and scattering. *Geochemistry, Geophysics, Geosystems*, *16*(10), 3343–3361. https://doi.org/10.1002/2015GC005993

Coney, P. J., & Reynolds, S. J. (1977). Cordilleran benioff zones. *Nature*, *270*(5636), 403–406. https://doi.org/10.1038/270403a0

Conrad, C. P., & Molnar, P. (1997). The growth of Rayleigh-Taylor-type instabilities in the lithosphere for various rheological and density structures. *Geophysical Journal International*, *129*(1), 95–112. https://doi.org/10.1111/j.1365-246X.1997.tb00939.x

Dalton, C. A., Ekström, G., & Dziewoński, A. M. (2008). The global attenuation structure of the upper mantle. *Journal of Geophysical Research: Solid Earth*, *113*(B9), B09303. https://doi.org/10.1029/2007JB005429

Dave, R., & Li, A. (2016). Destruction of the Wyoming craton: Seismic evidence and geodynamic processes. *Geology*, *44*(11), 883–886. https://doi.org/10.1130/G38147.1

DeCelles, P. G. (2004). Late Jurassic to Eocene evolution of the Cordilleran thrust belt and foreland basin system, western U.S.A. *American Journal of Science*, *304*(2), 105–168. https://doi.org/10.2475/ajs.304.2.105

Decelles, P. G., Gray, M. B., Ridgway, K. D., Cole, R. B., Srivastava, P., Pequera, N., & Pivnik, D. A. (1991). Kinematic history of a foreland uplift from Paleocene synorogenic conglomerate, Beartooth Range, Wyoming and Montana. *GSA Bulletin*, *103*(11), 1458–1475. https://doi.org/10.1130/0016-7606(1991)103<1458:KHOAFU>2.3.CO;2

Deng, Y., Byrnes, J. S., & Bezada, M. (2021). New insights into the heterogeneity of the lithosphere-asthenosphere system beneath South China from teleseismic body-wave attenuation. *Geophysical Research Letters*, *48*(6), e2020GL091654. https://doi.org/10.1029/2020GL091654

Dickinson, W. R., & Snyder, W. S. (1978). Plate tectonics of the Laramide orogeny.In *Geological Society of America Memoirs* (Vol. *151*, pp. 355–366). Geological Society of America. https://doi.org/10.1130/MEM151-p355

Durek, J. J., & Ekström, G. (1996). A radial model of anelasticity consistent with long-period surface-wave attenuation. *Bulletin of the Seismological Society of America*, *86*(1A), 144–158. https://doi.org/10.1785/BSSA08601A0144

Dziewonski, A. M., & Anderson, D. L. (1981). Preliminary reference Earth model. *Physics of the Earth and Planetary Interiors*, *25*(4), 297–356. https://doi.org/10.1016/0031-9201(81)90046-7

Egan, S. S., & Urquhart, J. M. (1993). Numerical modelling of lithosphere shortening: Application to the Laramide erogenic province, western USA. *Tectonophysics*, *221*(3), 385–411. https://doi.org/10.1016/0040-1951(93)90170-O

Erslev, E., & Koenig, N. (2009). Three-dimensional kinematics of Laramide, basement-involved Rocky Mountain deformation, USA: Insights from minor faults and GIS-enhanced structure maps. *Geological Society of America Memoir*, *204*, 125–150. https://doi.org/10.1130/2009.1204(06)

Erslev, E. A. (2005). 2D Laramide geometries and kinematics of the Rocky Mountains, Western U.S.A. *Geophysical Monograph Series*, *154*, 7–20. https://doi.org/10.1029/154GM02

Evans, R. L., Benoit, M. H., Long, M. D., Elsenbeck, J., Ford, H. A., Zhu, J., & Garcia, X. (2019). Thin lithosphere beneath the central Appalachian Mountains: A combined seismic and magnetotelluric study. *Earth and Planetary Science Letters*, *519*, 308–316. https://doi.org/10.1016/j.epsl.2019.04.046

Fan, M., & Carrapa, B. (2014). Late Cretaceous–early Eocene Laramide uplift, exhumation, and basin subsidence in Wyoming: Crustal responses to flat slab subduction. *Tectonics*, *33*(4), 509–529. https://doi.org/10.1002/2012TC003221

Gallegos, A., Ranasinghe, N., Ni, J., & Sandvol, E. (2014). Lg attenuation in the central and eastern United States as revealed by the EarthScope Transportable Array. *Earth and Planetary Science Letters*, *402*, 187–196. https://doi.org/10.1016/j.epsl.2014.01.049

Gallegos, A., Ranasinghe, N., Ni, J., & Sandvol, E. (2017). Lg attenuation, frequency dependence and relative site response of the western United States as revealed by the EarthScope Transportable Array. *Geophysical Journal International*, *209*(3), 1955–1971. https://doi.org/10.1093/gji/ggx145

Gao, S., Rudnick, R. L., Yuan, H.-L., Liu, X.-M., Liu, Y.-S., Xu, W.-L., et al. (2004). Recycling lower continental crust in the North China craton. *Nature*, *432*(7019), 892–897. https://doi.org/10.1038/nature03162

Griffin, W. L., Kobussen, A. F., Babu, E. V. S. S. K., O'Reilly, S. Y., Norris, R., & Sengupta, P. (2009). A translithospheric suture in the vanished 1-Ga lithospheric root of South India: Evidence from contrasting lithosphere sections in the Dharwar Craton. *Lithos*, *112*, 1109–1119. https://doi.org/10.1016/j.lithos.2009.05.015

Havlin, C., Holtzman, B. K., & Hopper, E. (2021). Inference of thermodynamic state in the asthenosphere from anelastic properties, with applications to North American upper mantle. *Physics of the Earth and Planetary Interiors*, *314*, 106639. https://doi.org/10.1016/j.pepi.2020.106639

Huang, J., Zhong, S., & van Hunen, J. (2003). Controls on sublithospheric small-scale convection. *Journal of Geophysical Research: Solid Earth*, *108*(B8), 2405. https://doi.org/10.1029/2003JB002456

Humphreys, E., Hessler, E., Dueker, K., Farmer, G. L., Erslev, E., & Atwater, T. (2003). How Laramide-age hydration of North American lithosphere by the farallon slab controlled subsequent activity in the Western United States. *International Geology Review*, *45*(7), 575–595. https://doi.org/10.2747/0020-6814.45.7.575

Humphreys, E. D., Schmandt, B., Bezada, M. J., & Perry-Houts, J. (2015). Recent craton growth by slab stacking beneath Wyoming. *Earth and Planetary Science Letters*, *429*, 170–180. https://doi.org/10.1016/j.epsl.2015.07.066

Jackson, I., & Faul, U. H. (2010). Grainsize-sensitive viscoelastic relaxation in olivine: Towards a robust laboratory-based model for seismological application. *Physics of the Earth and Planetary Interiors*, *183*(1), 151–163. https://doi.org/10.1016/j.pepi.2010.09.005

Jackson, W. T., Jr., McKay, M. P., Bartholomew, M. J., Allison, D. T., Spurgeon, D. L., Shaulis, B., et al. (2019). Initial Laramide tectonism recorded by Upper Cretaceous paleoseismites in the northern Bighorn Basin, USA: Field indicators of an applied end load stress. *Geology*, *47*(11), 1059–1063. https://doi.org/10.1130/G46738.1

Johnson, T. E., Brown, M., Kaus, B. J. P., & VanTongeren, J. A. (2014). Delamination and recycling of Archaean crust caused by gravitational instabilities. *Nature Geoscience*, *7*(1), 47–52. https://doi.org/10.1038/ngeo2019

Karato, S. (2008). *Deformation of earth materials. An introduction to the rheology of solid Earth* (p. 463). Cambridge University Press. https://doi.org/10.1017/cbo9780511804892

Karato, S., & Spetzler, H. A. (1990). Defect microdynamics in minerals and solid-state mechanisms of seismic wave attenuation and velocity dispersion in the mantle. *Reviews of Geophysics*, *28*(4), 399–421. https://doi.org/10.1029/RG028i004p00399

Kilian, T. M., Chamberlain, K. R., Evans, D. A. D., Bleeker, W., & Cousens, B. L. (2016). Wyoming on the run—Toward final Paleoproterozoic assembly of Laurentia. *Geology*, *44*(10), 863–866. https://doi.org/10.1130/G38042.1

Kirchner, J. G. (1977). Evidence for late tertiary volcanic activity in the Northern Black Hills, South Dakota. *Science*, *196*(4293), 977–977. https://doi.org/10.1126/science.196.4293.977

Kusky, T. M., & Li, J. (2003). Paleoproterozoic tectonic evolution of the North China Craton. *Journal of Asian Earth Sciences*, *22*(4), 383–397. https://doi.org/10.1016/S1367-9120(03)00071-3

Kusky, T. M., Windley, B. F., Wang, L., Wang, Z., Li, X., & Zhu, P. (2014). Flat slab subduction, trench suction, and craton destruction: Comparison of the North China, Wyoming, and Brazilian cratons. *Tectonophysics*, *630*, 208–221. https://doi.org/10.1016/j.tecto.2014.05.028

Lee, C.-T. A., Luffi, P., & Chin, E. J. (2011). Building and destroying continental mantle. *Annual Review of Earth and Planetary Sciences*, *39*(1), 59–90. https://doi.org/10.1146/annurev-earth-040610-133505

Lisenbee, A. L., DeWitt, E., & Snoke, A. W. (1993). *Laramide Evolution of the Black Hills Uplift*. (Vol. *5*, pp. 374–412). Geology of Wyoming: Geological Survey of Wyoming Memoir.

Liu, H., Byrnes, J. S., Bezada, M., Wu, Q., Pei, S., & He, J. (2021). *Variable depths of magma genesis in Eastern Asia inferred from teleseismic P wave attenuation [preprint]*. https://doi.org/10.1002/essoar.10507202.1

Malinverno, A., & Briggs, V. A. (2004). Expanded uncertainty quantification in inverse problems: Hierarchical Bayes and empirical Bayes. *Geophysics*, *69*(4), 1005–1016. https://doi.org/10.1190/1.1778243

Mazza, S. E., Gazel, E., Johnson, E. A., Kunk, M. J., McAleer, R., Spotila, J. A., et al. (2014). Volcanoes of the passive margin: The youngest magmatic event in eastern North America. *Geology*, *42*(6), 483–486. https://doi.org/10.1130/G35407.1

Montagner, J.-P., & Kennett, B. L. N. (1996). How to reconcile body-wave and normal-mode reference earth models. *Geophysical Journal International*, *125*(1), 229–248. https://doi.org/10.1111/j.1365-246X.1996.tb06548.x

Mueller, P. A., & Frost, C. D. (2006). The Wyoming Province: A distinctive Archean craton in Laurentian North America. *Canadian Journal of Earth Sciences*, *43*(10), 1391–1397. https://doi.org/10.1139/e06-075

Porter, R., Liu, Y., & Holt, W. E. (2016). Lithospheric records of orogeny within the continental U.S. *Geophysical Research Letters*, *43*(1), 144–153. https://doi.org/10.1002/2015GL066950

Pozgay, S. H., Wiens, D. A., Conder, J. A., Shiobara, H., & Sugioka, H. (2009). Seismic attenuation tomography of the Mariana subduction system: Implications for thermal structure, volatile distribution, and slow spreading dynamics. *Geochemistry, Geophysics, Geosystems*, *10*(4), Q04X05. https://doi.org/10.1029/2008GC002313

Ramos, V. A., Jordan, T. E., Allmendinger, R. W., Mpodozis, C., Kay, S. M., Cortés, J. M., & Palma, M. (1986). Paleozoic terranes of the central Argentine-Chilean Andes. *Tectonics*, *5*(6), 855–880. https://doi.org/10.1029/TC005i006p00855

Reiners, P. W., & Brandon, M. T. (2006). Using thermochronology to understand orogenic erosion. *Annual Review of Earth and Planetary Sciences*, *34*(1), 419–466. https://doi.org/10.1146/annurev.earth.34.031405.125202

Reiners, P. W., & Farley, K. A. (2001). Influence of crystal size on apatite (U–Th)/He thermochronology: An example from the Bighorn Mountains, Wyoming. *Earth and Planetary Science Letters*, *188*(3), 413–420. https://doi.org/10.1016/S0012-821X(01)00341-7

Riley, S., Degloria, S., & Elliot, S. D. (1999). A Terrain ruggedness index that quantifies topographic heterogeneity. *Internation Journal of Science*, *5*, 23–27.

Romanowicz, B., & Dziewonski, A. (2010). *Seismology and structure of the Earth: Treatise on Geophysics*. Elsevier.

Rychert, C. A., Fischer, K. M., Abers, G. A., Plank, T., Syracuse, E., Protti, J. M., et al. (2008). Strong along-arc variations in attenuation in the mantle wedge beneath Costa Rica and Nicaragua. *Geochemistry, Geophysics, Geosystems*, *9*(10), Q10S10. https://doi.org/10.1029/2008GC002040

Saleeby, J. (2003). Segmentation of the Laramide Slab—Evidence from the southern Sierra Nevada region. *GSA Bulletin*, *115*(6), 655–668. https://doi.org/10.1130/0016-7606(2003)115<0655:SOTLSF>2.0.CO;2

Schmandt, B., & Humphreys, E. (2010). Complex subduction and small-scale convection revealed by body-wave tomography of the western United States upper mantle. *Earth and Planetary Science Letters*, *297*(3), 435–445. https://doi.org/10.1016/j.epsl.2010.06.047

Schmandt, B., & Lin, F.-C. (2014). P and S wave tomography of the mantle beneath the United States. *Geophysical Research Letters*, *41*(18), 6342–6349. https://doi.org/10.1002/2014GL061231

Shah, A. K., & Boyd, O. S. (2018). *Depth to basement and thickness of unconsolidated sediments for the western United States—Initial estimates for layers of the U.S. Geological Survey National Crustal Model* (USGS Numbered Series No. 2018–1115). *Depth to basement and thickness of unconsolidated sediments for the western United States—Initial estimates for layers of the U.S. Geological Survey National Crustal Model* (Vol. 2018–1115). Geological Survey. https://doi.org/10.3133/ofr20181115

Shen, W., & Ritzwoller, M. H. (2016). Crustal and uppermost mantle structure beneath the United States. *Journal of Geophysical Research: Solid Earth*, *121*(6), 4306–4342. https://doi.org/10.1002/2016JB012887

Sheehan, A., Miller, K., Anderson, M., Siddoway, C. S., & Erslev, E. (2009). *Collaborative research: Geometry and kinematics of basement-involved foreland arches: Insights into continental processes from Earthscope*. https://doi.org/10.7914/SN/XV_2009

Simpson, R. W., Jachens, R. C., Blakely, R. J., & Saltus, R. W. (1986). A new isostatic residual gravity map of the conterminous United States with a discussion on the significance of isostatic residual anomalies. *Journal of Geophysical Research: Solid Earth*, *91*(B8), 8348–8372. https://doi.org/10.1029/JB091iB08p08348

Singleton, J. S., Mavor, S. P., Seymour, N. M., Williams, S. A., Patton, A. I., Ruthven, R. C., et al. (2019). Laramide shortening and the influence of Precambrian basement on uplift of the Black Hills, South Dakota and Wyoming, U.S.A. *Rocky Mountain Geology*, *54*(1), 1–17. https://doi.org/10.24872/rmgjournal.54.1.1

Small, E. E., & Anderson, R. S. (1998). Pleistocene relief production in Laramide mountain ranges, western United States. *Geology*, *26*(2), 123–126. https://doi.org/10.1130/0091-7613(1998)026<0123:PRPILM>2.3.CO;2

Soto Castaneda, R. A., Abers, G. A., Eilon, Z. C., & Christensen, D. H. (2021). Teleseismic attenuation, temperature, and melt of the upper Mantle in the Alaska subduction zone. *Journal of Geophysical Research: Solid Earth*, *126*(7), e2021JB021653. https://doi.org/10.1029/2021JB021653

Takei, Y. (2017). Effects of partial melting on seismic velocity and attenuation: A new insight from experiments. *Annual Review of Earth and Planetary Sciences*, *45*(1), 447–470. https://doi.org/10.1146/annurev-earth-063016-015820

Teng, T.-L. (1968). Attenuation of body waves and the Q structure of the mantle. *Journal of Geophysical Research*, *73*(6), 2195–2208. https://doi.org/10.1029/JB073i006p02195

Tikoff, B., & Maxson, J. (2001). Lithospheric buckling of the Laramide foreland during Late Cretaceous and Paleogene, western United States. *Rocky Mountain Geology*, *36*(1), 13–35. https://doi.org/10.2113/gsrocky.36.1.13

Toksöz, M. N., Dainty, A. M., Reiter, E., & Wu, R.-S. (1988). A model for attenuation and scattering in the Earth's crust. *Pure and Applied Geophysics*, *128*(1), 81–100. https://doi.org/10.1007/BF01772591

van Ravenzwaaij, D., Moore, C. P., Lee, M. D., & Newell, B. R. (2014). A hierarchical Bayesian modeling approach to searching and stopping in multi-attribute judgment. *Cognitive Science*, *38*(7), 1384–1405. https://doi.org/10.1111/cogs.12119

Wang, X., Zhao, D., & Li, J. (2016). The 2013 Wyoming upper mantle earthquakes: Tomography and tectonic implications. *Journal of Geophysical Research: Solid Earth*, *121*(9), 6797–6808. https://doi.org/10.1002/2016JB013118

Wang, Y., Zhou, L., & Zhao, L. (2013). Cratonic reactivation and orogeny: An example from the northern margin of the North China Craton. *Gondwana Research*, *24*(3), 1203–1222. https://doi.org/10.1016/j.gr.2013.02.011

Wei, S. S., & Wiens, D. A. (2020). High bulk and shear attenuation due to partial melt in the Tonga-Lau Back-arc mantle. *Journal of Geophysical Research: Solid Earth*, *125*(1), e2019JB017527. https://doi.org/10.1029/2019JB017527

West, J. D., Fouch, M. J., Roth, J. B., & Elkins-Tanton, L. T. (2009). Vertical mantle flow associated with a lithospheric drip beneath the Great Basin. *Nature Geoscience*, *2*(6), 439–444. https://doi.org/10.1038/ngeo526

Whitmeyer, S. J., & Karlstrom, K. E. (2007). Tectonic model for the Proterozoic growth of North America. *Geosphere*, *3*(4), 220–259. https://doi.org/10.1130/GES00055.1

Worthington, L. L., Miller, K. C., Erslev, E. A., Anderson, M. L., Chamberlain, K. R., Sheehan, A. F., et al. (2016). Crustal structure of the Bighorn Mountains region: Precambrian influence on Laramide shortening and uplift in north-central Wyoming. *Tectonics*, *35*(1), 208–236. https://doi.org/10.1002/2015TC003840

Xie, J., Chu, R., & Yang, Y. (2018). 3-D upper-mantle shear velocity model beneath the contiguous United States Based on broadband surface wave from ambient seismic noise. *Pure and Applied Geophysics*, *175*(10), 3403–3418. https://doi.org/10.1007/s00024-018-1881-2

Yeck, W. L., Sheehan, A. F., Anderson, M. L., Erslev, E. A., Miller, K. C., & Siddoway, C. S. (2014). Structure of the Bighorn Mountain region, Wyoming, from teleseismic receiver function analysis: Implications for the kinematics of Laramide shortening. *Journal of Geophysical Research: Solid Earth*, *119*(9), 7028–7042. https://doi.org/10.1002/2013JB010769

Zhu, R., Xu, Y., Zhu, G., Zhang, H., Xia, Q., & Zheng, T. (2012). Destruction of the North China craton. *Science China Earth Sciences*, *55*(10), 1565–1587. https://doi.org/10.1007/s11430-012-4516-y